Materials Today Bio 33 (2025) 101985

Contents lists available at ScienceDirect

Materials Today Bio

journal homepage: www.journals.elsevier.com/materials-today-bio

Efficient on-demand cuproptosis induction against triple-negative breast cancer via dual-responsive black phosphorus nanosheet

Qiancun Hong [a,c,d,2], Jiajun Huang [b,c,2], Zhiguo Li [b,c,2], Yue Chen [b,c], Jiawei Wang [a,b,c,d], Tongrui Shang [b,c], Zelin Chen [c], Cong Luo [c], Yongqiang Wang [c], Xinghong Tang [b,c], Taojian Fan [f,*], Songyin Huang [e,**], Hao Fu [a,c,***], Yandan Yao [a,b,c,d,1]

[a] Shenshan Medical Center, Sun Yat-sen Memorial Hospital, Sun Yat-sen University, Shanwei, China
[b] Breast Tumor Center, Sun Yat-sen Memorial Hospital, Sun Yat-sen University, Guangzhou, China
[c] Guangzhou Key Laboratory of Medical Nanomaterials, Guangdong Provincial Key Laboratory of Malignant Tumor Epigenetics and Gene Regulation, Guangdong-Hong Kong Joint Laboratory for RNA Medicine, Medical Research Center, Sun Yat-Sen Memorial Hospital, Sun Yat-Sen University, Guangzhou, China
[d] Guangdong Provincial Key Laboratory of Cancer Pathogenesis and Precision Diagnosis and Treatment, Shenshan Medical Center, Sun Yat-sen Memorial Hospital, Sun Yat-sen University, Shanwei, Guangdong, China
[e] Biotherapy Center, Sun Yat-sen Memorial Hospital, Sun Yat-sen University, Guangzhou, China
[f] Dongguan Key Laboratory of Sepsis Translational Medicine, The First Dongguan Affiliated Hospital, Guangdong Medical University, Dongguan, China

ARTICLE INFO

Keywords:
Triple-negative breast cancer
Cuproptosis
On-demand
Black phosphorus nanosheets
Dual-responsive
Fenton-like reaction

ABSTRACT

Cuproptosis, a newly identified cell death pathway, has been shown by our analyses to be closely associated with the clinical prognosis of triple-negative breast cancer (TNBC) patients and may potentially facilitate the elimination of TNBC. However, precisely and efficiently regulating cuproptosis in tumor regions in a controllable manner remains challenging. Here, a highly effective cuproptosis inducer based on black phosphorus nanosheets (BPNs@Cu@PDA, denoted as BCP) is constructed, featuring acidic and thermal-responsive copper ion release, as well as enhanced cuprous ion (Cu^{+}) loading capability. Briefly, BCP efficiently increases the loading proportion of Cu^{+} via inherent surface redox reactions between phosphorus and copper ions (Cu^{2+}), thereby enabling a significantly elevated cuproptosis induction ability. After accumulating at the tumor, BCP precisely releases $Cu^{+/2+}$ in response to the photo-hyperthermia and acidic microenvironment created by the dopamine modification, thereby efficiently producing reactive hydroxyl radicals (•OH) through $Cu^{+/2+}$-dependent Fenton-like reactions, which leads to significant oxidative damage in TNBC cells. The precisely released $Cu^{+/2+}$ further inhibits the production of the Fe-S cluster while causing the aggregation of succinylated proteins, leading to significantly disrupted mitochondrial function and the TCA cycle, thereby inducing significant cuproptosis and subsequent TNBC suppression (over 90 % decrease in tumor volumes) in a synergistic manner. This research presents a novel cuproptosis induction strategy specifically designed for TNBC that has negligible toxicity, which may provide insights into the clinical treatment of TNBC.

1. Introduction

Breast cancer (BC) [1–3] stands as one of the predominant causes of mortality among women globally. Conventional interventions, including surgery [4], chemotherapy [5], and radiation therapy [6], have significantly improved the prognosis of patients. However, the complexity, diversity, and heterogeneity of breast carcinoma prevent conventional interventions from achieving optimal efficacy and may subsequently result in multiple adverse effects. Therefore, an urgent request for alternative novel synergistic therapeutic strategies is calling

* Corresponding author.
** Corresponding author.
*** Corresponding author. Shenshan Medical Center, Sun Yat-sen Memorial Hospital, Sun Yat-sen University, Shanwei, China.
E-mail addresses: fantaojian@gdmudgah.com (T. Fan), huangsy@mail.sysu.edu.cn (S. Huang), fuhao28@mail.sysu.edu.cn (H. Fu).
[1] Prof. Yandan Yao deceased on Nov. 21st, 2024.
[2] These authors contributed equally to this work.

https://doi.org/10.1016/j.mtbio.2025.101985
Received 31 March 2025; Received in revised form 7 June 2025; Accepted 12 June 2025
Available online 13 June 2025

[7,8]. Nevertheless, cuproptosis [9–14] is a copper ion-dependent form of regulated cell death, identified by Peter Tsvetkov in 2022 [15]. It depends on the accumulation of copper ions within cells, especially the monovalent copper ions (Cu^{+}), which directly bind to succinylated proteins in the TCA cycle [16,17], leading to cell death caused by protein aggregation and dysfunction [18–21]. Interestingly, analysis of transcriptional profiles and clinical information uncovered that the cuproptosis-related transcriptional profiles are highly correlated with the prognosis and survival of TNBC patients (Figs. 1 and 2). Thus, leveraging the cuproptosis-inducing effect of copper ions may provide new insights for overcoming the currently unsatisfactory therapeutic outcome of TNBC. However, the toxicity attributed to the high reactivity of free copper ions strongly limits the development of cuproptosis-based therapies.

Photothermal therapy (PTT) ablate tumor cells by transform light energy into heat, which can also preferentially enhance the permeability and fluidity of cell membranes, thereby increasing the cellular uptake of drugs or nanomedicine [22,23]. Moreover, inspired by nanocatalytic medicine, metal ions with variable valence can catalyze in situ Fenton or Fenton-like reactions for enhanced tumor inhibition [24–26]. For example, Cu^{+} can respond to the tumor microenvironment and thus convert hydrogen peroxide (H_2O_2) into highly toxic reactive oxygen species (ROS) [28–30], such as hydroxyl radicals (•OH) [31,32], resulting in significant tumor killing with high selectivity. Therefore, developing a multifunctional nanoplatform for therapeutics that integrates photothermal and controllable copper ion release properties holds great promise for safe and on-demand breast cancer inhibition. Unfortunately, current attempts have consistently yielded unsatisfactory therapeutic outcomes for TNBC via cuproptosis due to inadequate loading and antioxidant protection of Cu^{+}, insufficient photothermal conversion, and a limited response to the tumor-microenvironment (TME) [33,34]. Thus, a nanoplatform with high NIR photothermal conversion efficiency requires a large proportion of Cu^{+} loading capacity and controllable ion release.

Black phosphorus two-dimensional nanosheets (BPNs) [35–37], which exhibit exceptional electrochemical and optical properties, along with excellent bioactivity and biocompatibility, have garnered significant attention for years. Studies have demonstrated that BPNs, as a metal-free lamellar semiconductor, exhibit an absorption spectrum spanning from the ultraviolet to visible light regions endowed by the thickness-dependent tunability of the bandgap ranging from approximately 0.3 eV in bulk to 2.0 eV in monolayer form, thereby displaying high near-infrared (NIR) photothermal conversion capability suitable for photothermal therapy (PTT). The rumpled lattice structure of BPNs

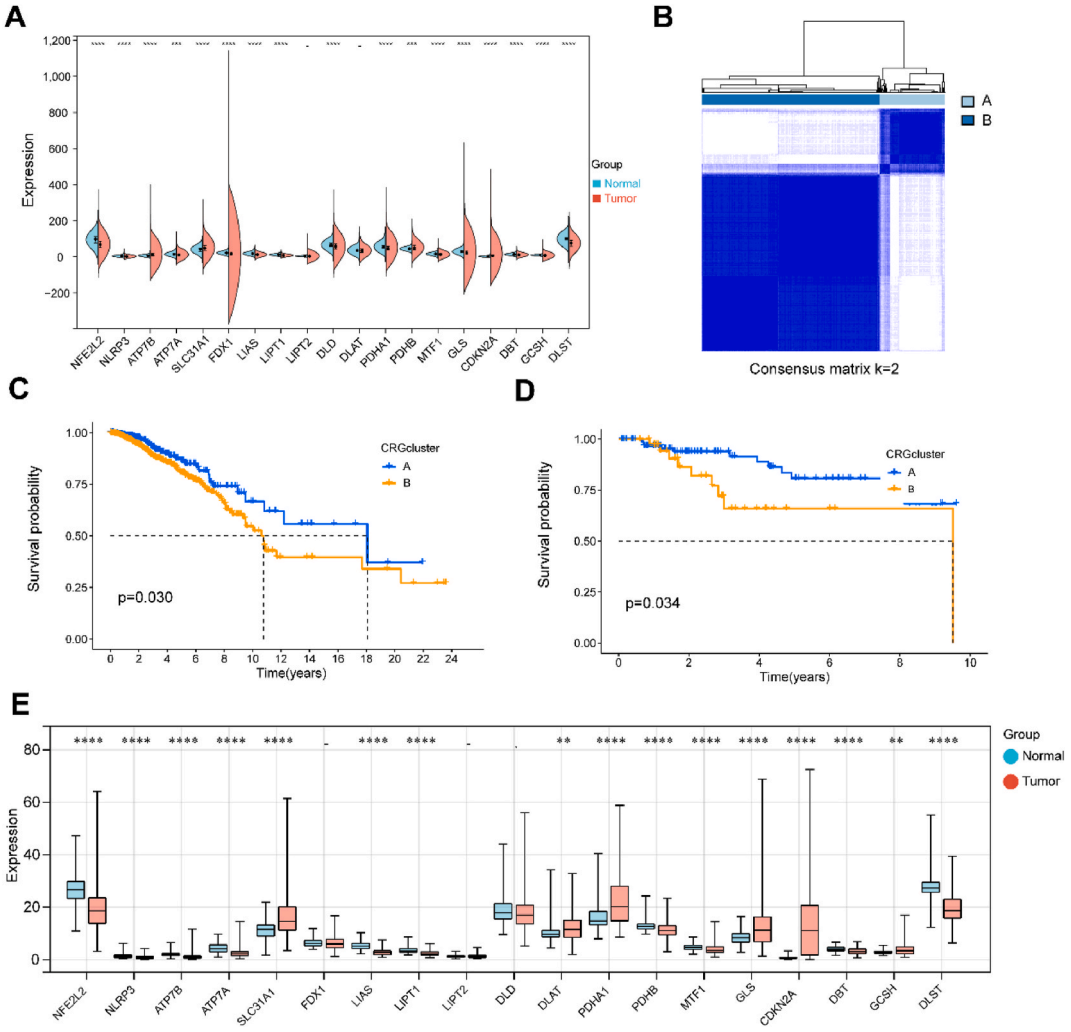

Fig. 1. Cuproptosis-related pathways are significantly associated with prognosis in triple-negative breast cancer (TNBC). (A) Differential expression of cuproptosis-related genes (CRGs) between tumor and adjacent normal tissues in breast cancer. (B) Consensus clustering analysis stratified breast cancer patients into two molecular subtypes with distinct characteristics. (C) Kaplan-Meier survival analysis of overall survival (OS) across molecular subtypes in the overall breast cancer cohort. (D) Kaplan-Meier survival analysis of OS in TNBC-specific molecular subgroups. (E) Differential expression of CRGs between tumor and adjacent normal tissues in TNBC.

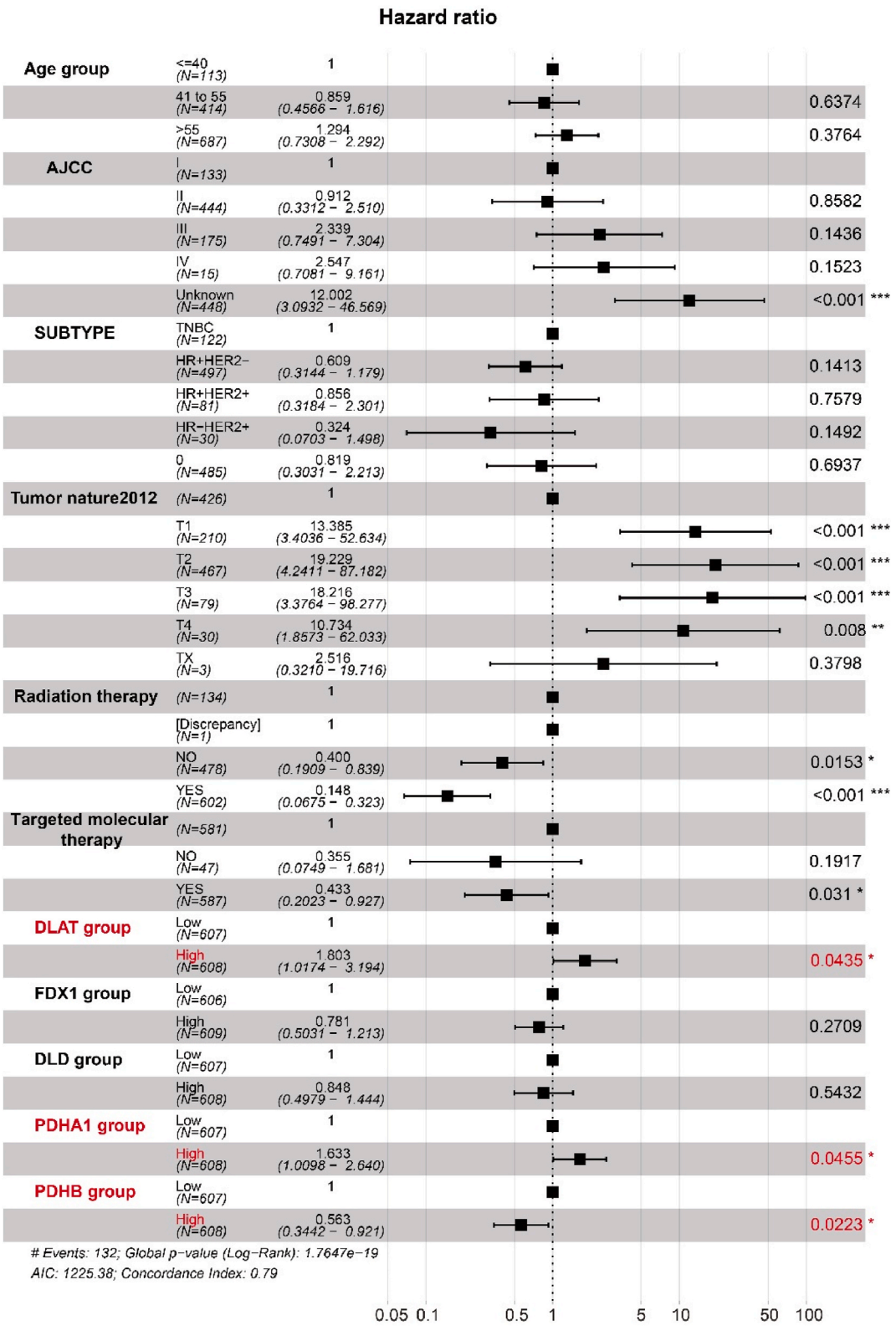

Fig. 2. Univariate Cox regression analysis of the relationship between the core genes related to cuproptosis and prognosis in BC patients. Results are displayed using forest plots. The cuproptosis-related genes with significant differences are highlighted in red. (For interpretation of the references to color in this figure legend, the reader is referred to the Web version of this article.)

also exhibits a larger specific surface area compared to conventional two-dimensional materials [38], such as graphene and MoS_2, thus significantly enhancing the loading capacity of BPNs, particularly for metal ions like Cu^{2+} or Cu^{+}. Furthermore, the highly reductive nature of phosphorus substantially improves the loading proportion of Cu^{+} through an inherent surface reductive reaction, thereby considerably boosting the efficacy of cuproptosis induction. Such unique structures and physicochemical properties suggest that BPNs can be considered an

optimal multifunctional nanoplatform for on-demand TNBC inhibition via triggering cuproptosis.

Herein, a novel black phosphorus nanosheet-based cuproptosis inducer (BCP) is constructed according to our findings on the correlation between cuproptosis and TNBC patients (Scheme 1). Briefly, BCP efficiently loads a large proportion of Cu^{+} by inherent surface redox reactions of BPNs. Moreover, the polydopamine (PDA) [39,40], modified on the surface of BCP, enables an enhanced photothermal transition and pH response without unwanted copper ion leakage. BCP precisely releases $Cu^{+/2+}$ in response to NIR and the acidic microenvironment in tumor regions, thereby promoting reactive hydroxyl radicals (•OH) through Fenton-like reactions, which leads to enhanced tumor cell death. The released Cu^{+} further binds to proteins, such as DLAT, resulting in a disrupted TCA cycle due to protein aggregation and subsequently inhibiting TNBC progression through the emergence of cuproptosis. Results demonstrate that *in vitro* and *in vivo* TNBC progression was significantly prevented by this cuproptosis induction strategy, which offers high biosafety and may overcome the bottleneck in TNBC therapy.

2. Results

2.1. Analysis of cuproptosis-related transcriptional profiles and corresponding prognosis in the clinical database

The prognostic value of cuproptosis-related genes (CRGs) in patients with BC was systematically evaluated. As shown in Fig. 1A, TCGA database analysis revealed significant differential expression of most CRGs (e.g., DLAT, PDHA1, PDHB) in tumor tissues compared to normal tissues ($P < 0.05$). Based on the expression profiles of these genes, the consensus clustering algorithm classified BC patients into two molecular subgroups with distinct characteristics (Fig. 1B), and Kaplan-Meier survival analysis demonstrated significant differences in overall survival (OS) between the two groups ($P = 0.03$) (Fig. 1C). Given the high heterogeneity and limited therapeutic options in triple-negative breast cancer (TNBC), we further focused on this subtype. Kaplan-Meier analysis in TNBC patients also revealed a significant association between CRGs and prognosis ($P = 0.03$), consistent with findings in the overall breast cancer (BC) cohort (Fig. 1D). Differential expression analysis further confirmed significantly upregulated levels of DLAT and PDHA1 and downregulated PDHB in TNBC tumor tissues (Fig. 1E)

Moreover, Univariate Cox regression analysis also revealed the prognostic significance of core genes: high expression of DLAT (HR = 1.83, 95 % CI: 1.02–3.19) and PDHA1 (HR = 1.63, 95 % CI: 1.01–2.64) correlated with poor outcomes, whereas high PDHB expression exhibited a protective effect (HR = 0.56, 95 % CI: 0.34–0.92) (Fig. 2). These findings suggest that targeting copper metabolic pathways (e.g., inhibition of DLAT and PDHA1 or activation of PDHB) may offer novel therapeutic strategies for TNBC. Therefore, leveraging efficient and on-demand cuproptosis induction could hold promising prospects for TNBC suppression.

2.2. Preparation and characterization of BCP

Black phosphorus nanosheet (BPNs) with an average diameter of approximately 200 nm and an average thickness of about 4 nm were prepared via a liquid-phase ultrasonic exfoliation method (Figs. S1A, S2A, S2B). The TEM, Raman spectra, and X-ray photoelectron spectroscopy (XPS) results further indicated the successful synthesis of BPNs (Figs. S1B, C, S2C, D). The absorbance spectra also confirmed the NIR absorbance ability of BPNs (Fig. S1D). Then, copper ions (Cu^{2+}) were loaded onto the BPNs through stirring and adsorption centrifugation under a specific ratio (BPNs: Cu^{2+} = 3:1–30:1). To further reduce the copper ions leakage and subsequent systemic toxicity, PDA with reactive functional groups was encapsulated onto the copper ion-loaded BPNs by the spontaneous polymerization of dopamine monomers under alkaline conditions, according to a previous report [41], and BCP is obtained therein (Fig. 3A inserted). Transmission electron microscopy (TEM)

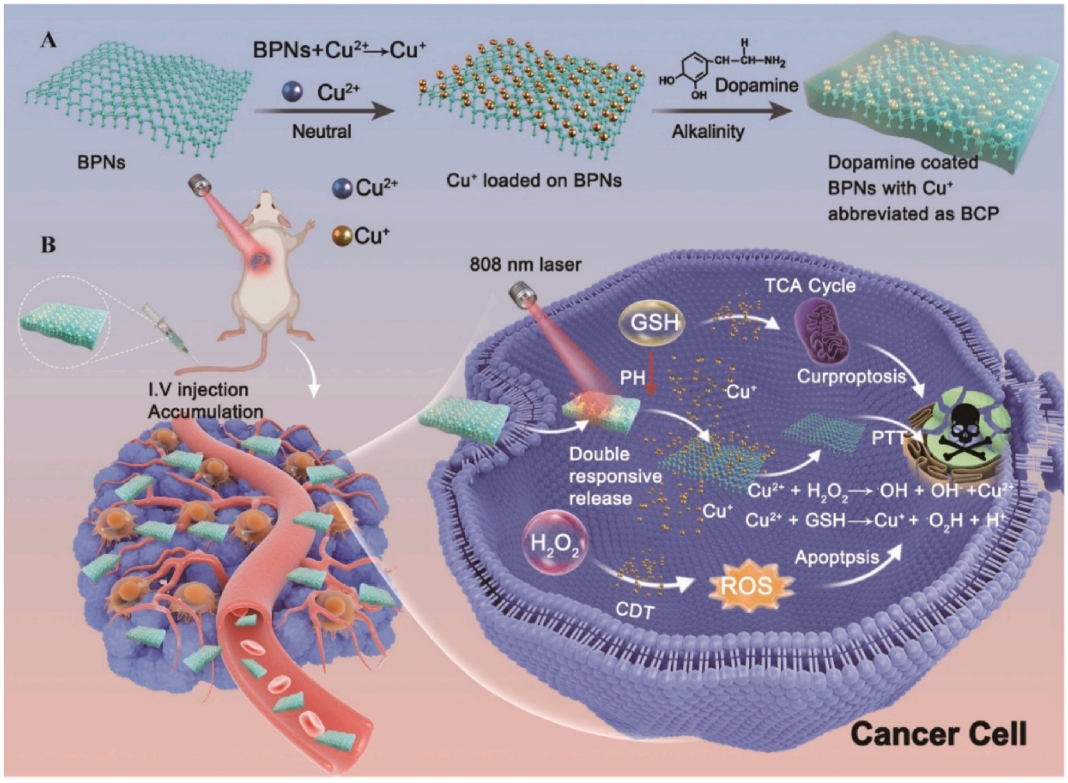

Scheme 1. (A) Illustration of the preparation process of BCP. (B) Schematic illustration of the efficient and on-demand induction of cuproptosis in TNBC using the dual-responsive BCP.

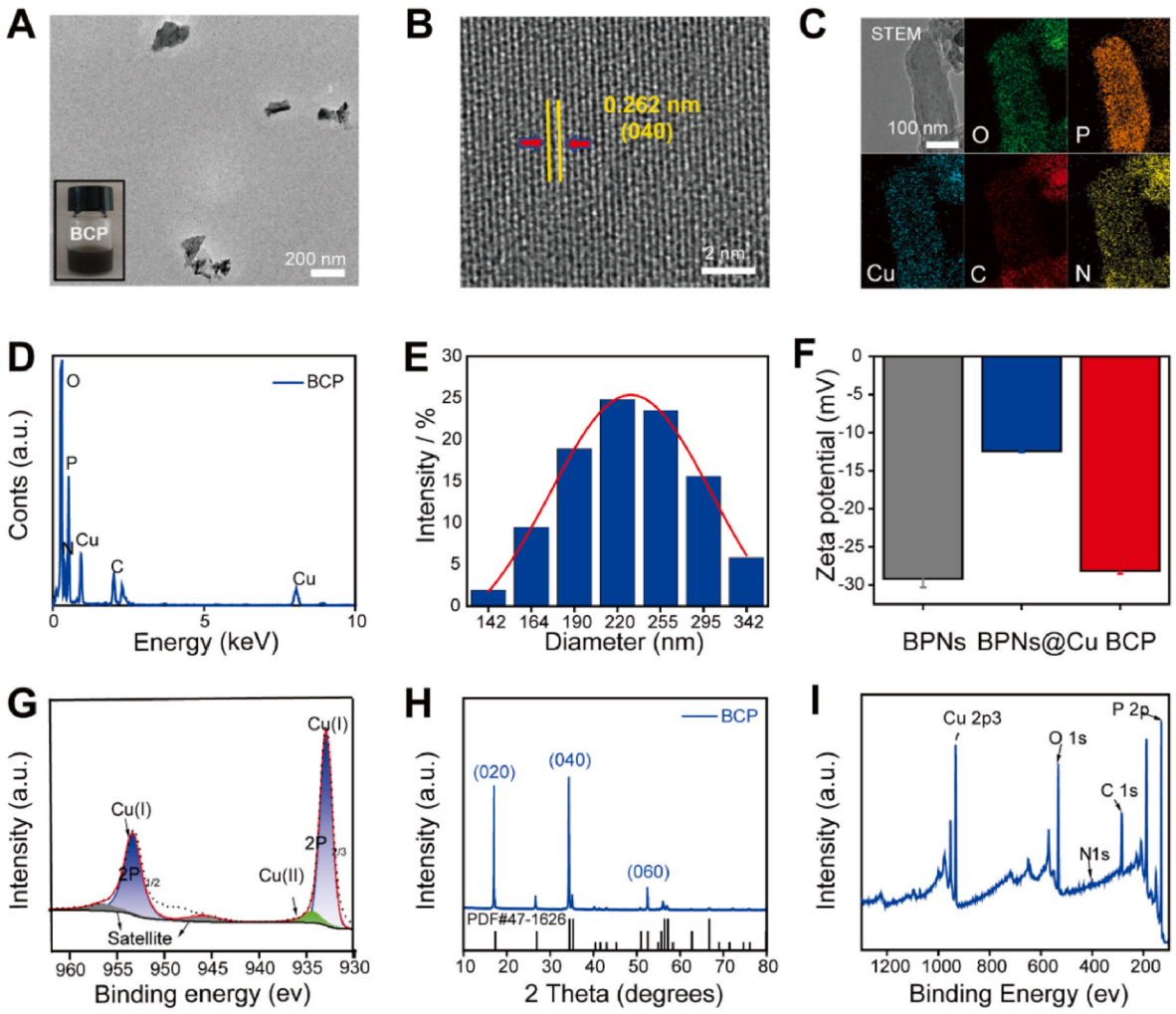

Fig. 3. Characterization of BCP. (A) TEM image of BCP (Inserted: BCP solution image). (B) High-resolution TEM image of BCP. (C) Elemental mapping and (D) the corresponding EDS spectra of BCP. (E) Size distribution of BCP measured by DLS. (F) Zeta-potential profiles of BPNs, BPNs@Cu, and BCP. (G) XPS spectra showing the binding energy of Cu2P in BCP. (H) X-ray diffraction (XRD) pattern and (I) XPS spectra of BCP.

images revealed that BCP exhibited a lamellar morphology with uniform dimensions, approximately 200 nm in diameter and 200 nm in length (Fig. 3A). Dynamic light scattering (DLS) analysis corroborated the TEM measurements, revealing an average BCP hydrodynamic diameter of approximately 220 nm (Fig. 3E). High-resolution transmission electron microscopy (HR-TEM) images (Fig. 3B, Fig. S4) further demonstrated a lattice spacing of 0.262 nm for BCP, aligning with the (040) plane of BPNs (Fig. S1C) [42], which presents an orderly striated pattern. X-ray diffraction (XRD) patterns (Fig. 3H, Fig. S5) corroborate the orderly striated pattern in the lattice spacing characteristic of the synthetic BCP composite. Moreover, high-angle annular dark-field scanning transmission electron microscopy (HAADF-STEM) images and corresponding elemental mapping images elucidated that copper was uniformly distributed in BPNs (Fig. 3C). Meanwhile, the PDA coating, as indicated in Fig. S3, is about 30 nm thick. The successful loading of copper ions onto BCP was further confirmed by a marked shift in zeta potential (Fig. 3F), shifting from −28 (BPNs) to −12 mV (BPNs@Cu), attributed to the adsorption of positively charged copper ions. However, the zeta potential of BPNs@Cu changed from −12 to −26 mV (BCP) upon encapsulation with dopamine, primarily due to the negatively charged particles provided by dopamine under alkaline conditions. Furthermore, energy-dispersive X-ray spectroscopy (EDS) (Fig. 3D) and X-ray photoelectron spectroscopy (XPS) (Fig. 3I) demonstrate the presence of Cu and N elements. The XPS spectrum of BCP revealed a notable N peak, indicating the existence of amino groups after PDA modification. The significant Cu 2p3 peak represents the Cu element, further validating the successful loading of $Cu^{+/2+}$. Additionally, two peaks, positioned at 530.75 and 285.35 eV, in the XPS spectrum of BCP were ascribed to C=O and C=N, respectively, further verifying the successful encapsulation of the dopamine shell. Moreover, in the XPS deconvolution graph (Fig. 3G), the satellite peaks corresponding to Cu^{2+} (962.5 and 942.7 eV) are barely detectable. On the contrary, the representative peaks indicating Cu^{+} (2p3/2 at 952.2 eV, 2p1/2 peak at 955.2 eV) are markedly observed. Such a result confirms the formation of Cu=O bonds, suggesting the abundant production of Cu $^{+}$ resulting from the redox reaction between Cu^{2+} and P, as shown in reaction equation (1) [38], which may significantly promote the induction of cuproptosis.

$$Cu^{2+} + P + 4OH^{-} \rightarrow Cu^{+} + PO_4^{3-} + 4H^{+} \quad (1)$$

In conclusion, the results indicate the successful synthesis of BCP, which may facilitate the induction of cuproptosis and ROS production by a Fenton-like reaction generated from an enhanced loading proportion of Cu^{+}.

2.3. Dual response and ROS production efficiency of BCP

An infrared thermal imager was utilized to monitor temperature changes under different conditions and evaluate the photothermal

efficiency of BCP. The temperature of the BCP solution increased in a concentration- and laser-energy-dependent manner (Fig. 4A and B). In contrast, the control group, which consisted of pure deionized water, displayed a negligible temperature change after 10 min of irradiation at 1 W/cm^2. This result demonstrates that the pronounced cumulative photothermal effect of BCP likely accounts for the excellent photothermal transition ability of BPNs and the PDA modification. Moreover, there was no significant temperature decay after five photothermal rounds of laser on/off cycles for BCP, indicating the excellent photothermal stability of this multifunctional nanoplatform (Fig. 4C, Fig. S7A). We have also compared the photothermal conversion efficiency of BPNs and BCP through experiments. The results showed that BCP achieved a photothermal conversion efficiency of 39.3 %, which is 3.2 % significantly higher than that of BPNs. This improvement may primarily be attributed to the effect of dopamine encapsulation, which enhances the photothermal conversion rate (Fig. S6). To further investigate the stability and dispersibility of the material, we conducted experiments by placing BCP in different solutions, including PBS (Fig. S13), DMEM (Fig. S14), and FBS (Fig. S15). The samples were continuously observed for over 7 days, and electronic photographs were collected. The corresponding results indicated that BCP exhibited excellent stability, with no sedimentation observed throughout the entire period. In addition, the Tyndall effect (Fig. S12) and dynamic light scattering experiments (Figure S16 and 17) further confirmed that the material possesses exceptional stability and dispersibility. Overall, the as-prepared BCP exhibits a high photothermal conversion capability and good stability, laying the foundation for further examination.

The cumulative ion release profile was then evaluated under various conditions at different time intervals (0, 2, 4, 6, 12, and 24 h); the collected supernatants from each group were quantified using ICP-MS. Results indicated that nearly no copper ions are released under pH 7.4 conditions, suggesting the high biocompatibility of BCP for stability and negligible copper ions leakage in normal physiological microenvironment (Fig. 4D, Fig. S5). However, a significant Cu ion release profile was observed in BCP under the pH 6.5 + laser condition, indicating the excellent dual-responsive release profile of BCP, enabling the on-

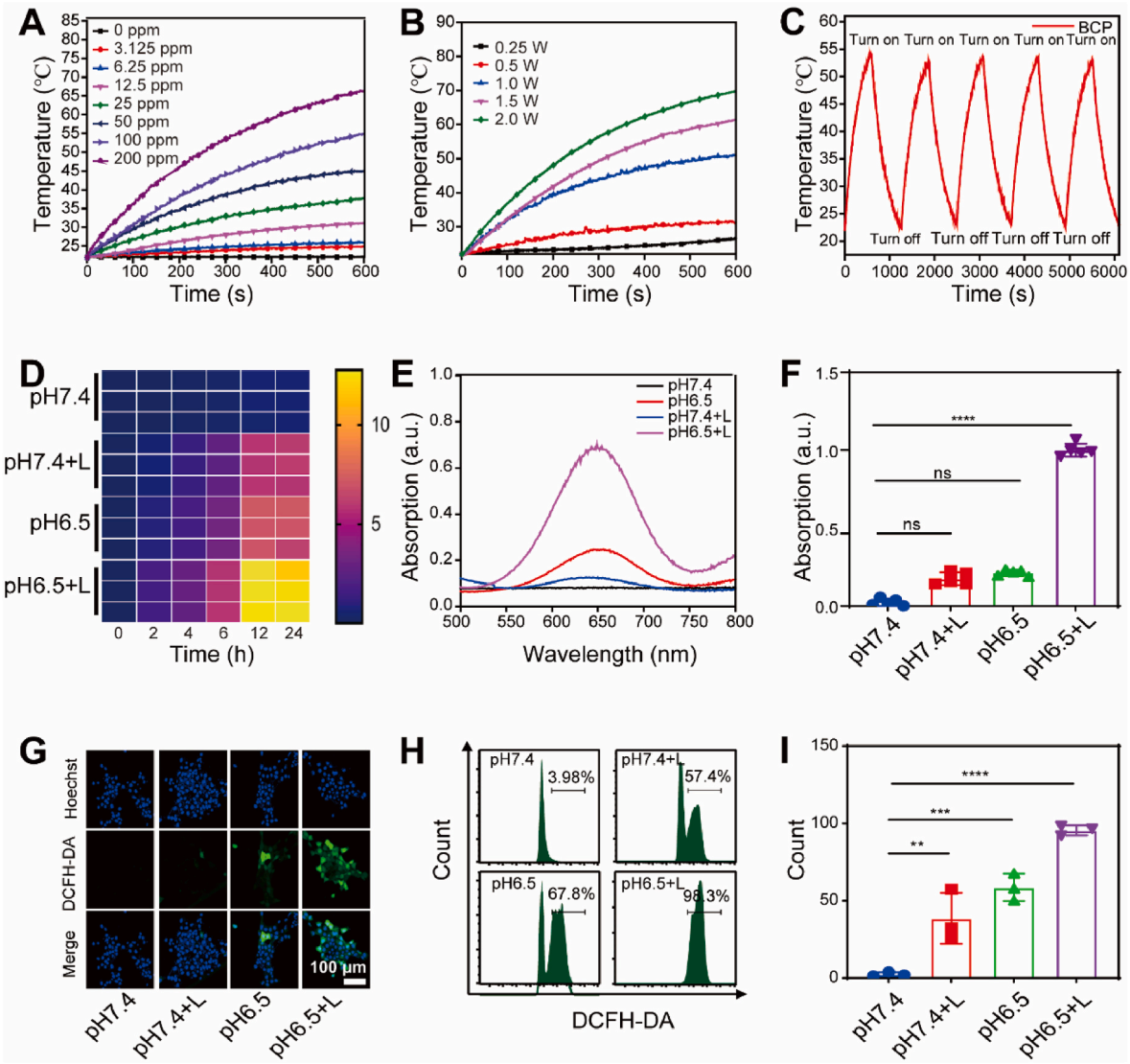

Fig. 4. Evaluation of the dual-responsive effects of BCP. (A) Temperature-time curves of BCP at various concentrations under NIR irradiation (808 nm, 1 W/cm^2). (B) Temperature-time curves of BCP under different irradiation powers. (C) The temperature-time curves of BCP after the laser was turned on and off 5 times. (D) The release profiles of Cu ions in response to NIR irradiation or acidic conditions. (E) ROS production efficiency quantified by the TMB absorbances and (F) the related quantification. Data are shown as mean ± S.D. (n = 5). (G) Intracellular ROS probe (DCFH-DA) captured by confocal microscopy after different treatments; scale bar: 20 μm. (H) Flow cytometry for ROS probe (DCFH-DA) detection in 4T1 cells following different treatments, with relative quantification. Data are shown as mean ± S. D. (n = 5). Statistics were calculated with the Student's t-test: *: $p < 0.05$, **: $p < 0.01$, ***: $p < 0.001$, ****: $p < 0.0001$. ns, not significant.

demand and precise cuproptosis induction under TME (Fig. 4D, Fig. S8). For assessment of the efficiency of dual-responsive ROS generation by $Cu^{+/2+}$ according to reaction equation (2) [43–45], the TMB experiment was leveraged based on the principle that TMB reacts with highly oxidative hydroxyl radicals (•OH) and forms oxidized TMB (ox-TMB) upon losing an electron, where the reaction product exhibits a distinct characteristic absorption peak at approximately 652 nm under the UV/Vis/NIR absorption spectrum (Fig. S9A and B). In the pH 7.4 group, after a 10-min incubation with TMB and H_2O_2 substrate, there was virtually no absorption, indicating minimal generation of •OH radicals (Fig. 4E, F, Fig. S9C). The pH 6.5 group and pH 7.4 + Laser group demonstrated moderate absorption at 652 nm, suggesting the production of a small amount of •OH radicals (Fig. 4E, F, Fig. S9C). In comparison to other groups, the pH 6.5 + Laser group exhibited the highest absorbance at 652 nm due to the cleavage of Cu=O bonds and disassembly of the dopamine layer on BCP in response to acidic conditions and laser irradiation, leading to a large amount of $Cu^{+/2+}$ release, which thus catalyzes H_2O_2 to generate •OH and react with TMB to form product characterized by absorbance peak at 652 nm (Fig. 4E, F, Fig. S9C). The decolorization of MB further demonstrated that the pH 6.5 + Laser group generated significant hydroxyl radicals (•OH), leading to significant MB degradation and a decrease in absorbance at 664 nm (Figs. S10 and S11). These experimental results substantiated that the prepared BCP possesses pH and photothermal dual-responsive effects.

$$Cu^{+} + H_2O_2 \rightarrow Cu^{2+} + \bullet OH + OH^{-} \quad (2)$$

The generation efficiency of ROS due to the Fenton-like reaction catalyzed by $Cu^{+/2+}$ is further evaluated using DCFH-DA (green fluorescence indicating the presence of ROS) staining and laser confocal fluorescence microscopic observation. Results displayed negligible green fluorescence under physiological conditions (pH 7.4 and 37 °C) (Fig. 4G), indicating enhanced prevention of $Cu^{+/2+}$ leakage after PDA modification. This is mainly because PDA forms a dense, cohesive polymer layer in a neutral microenvironment, thereby firmly restraining the release of $Cu^{+/2+}$ from BPNs [46–48]. However, under the acidic conditions (pH = 6.5) while exposure to NIR (808 nm, 1 W/cm^2, 10 min), the intensity of green fluorescence (DCFH-DA positive) is notably increased, suggesting the marked ROS production resulted from the dual-responsive release of $Cu^{+/2+}$ due to the collapse of the PDA polymer layer in response to acidic pH and NIR. Flow cytometry analysis further confirms the abundant production of ROS under acidic pH and photothermal conditions (Fig. 4H and I). These results demonstrate the effective, precise, and on-demand release of $Cu^{+/2+}$ to tumor regions of BCP, which may serve as a highly efficient inducer of cuproptosis for inhibiting TNBC tumors.

2.4. *In vitro antitumor efficiency of BCP and related mechanism investigation*

Under the fluorescence microscope imaging, the FITC-labeled BCP (green) can be efficiently internalized by 4T1 cells (blue) in a time-dependent manner (Fig. S18). As indicated by the cytotoxicity assay (CCK-8) on the TNBC cell line (4T1), BCP showed negligible toxicity, even at concentrations as high as 50 ppm, under normal physiological conditions (pH = 7.4) (Fig. S7B), suggesting excellent biosafety, which accounts for the limited $Cu^{+/2+}$ leakage. On the contrary, when subjected to acidic pH and NIR, BCP exhibits a significantly enhanced 4T1 cell-killing ability, which may result from the responsive release of $Cu^{+/2+}$ and subsequently lead to cuproptosis induction and ROS production. To validate the related molecular mechanisms of this phenomenon caused by BCP under acidic pH and NIR, RNA sequencing (RNA-seq) analysis was conducted on 4T1 cells after different treatments. The individual datasets of gene expression values from the various treatment groups exhibited significant clustering. Principal Component 1 (PC1) accounted for 76.6 % of the total variance, indicating that gene expression underwent substantial alterations in the BCP and BCP + Laser groups compared to the control group (Fig. 5A). Differential analysis of these shared genes revealed a volcano plot illustrating similar and pronounced upregulation and downregulation of gene expression in the BCP and BCP + Laser groups over the control group (Fig. 5B, C, Fig. S19), suggesting that these treatments trigger significant alterations in TNBC. Based on the Gene Ontology (GO) enrichment analysis, we discovered that the BCP and BCP + Laser markedly alter the cuproptosis-related biological processes, such as the regulation of the cellular catabolic process, response to oxygen levels or hypoxia, respiratory electron transport chain, indicating the cuproptosis induction that leading to the modulation of the cellular metabolism processes, mitochondria-related cellular respiration and the oxidation-reduction balance by these treatments [19,49,50]. Moreover, the BCP + Laser triggered more marked changes in the regulation of the protein catabolic process, ATP metabolic process, proton motive force−driven mitochondrial ATP synthesis, and the electron transport chain compared to the BCP and control groups (Fig. S20). Such a result strongly suggests that the BCP + Laser group triggers a burst of ROS and cuproptosis, subsequently leading to the malfunctions of mitochondria and the tricarboxylic acid (TCA) cycle [19,49,50]. Moreover, Kyoto Encyclopedia of Genes and Genomes (KEGG) pathway enrichments revealed that the BCP group regulated the signaling pathways closely linked to cuproptosis, such as oxidative stress, cell death, and cellular metabolism processes disrupted by cuproptosis, including HIF−1 signaling pathway, glycosphingolipid biosynthesis, autophagy, necroptosis, AMPK signaling pathway, compared to the control group (Fig. 5G) [51,52]. In addition, more biological pathways associated with cuproptosis and the TCA cycle influenced by cuproptosis, specifically the pyruvate metabolism, carbon metabolism, oxidative phosphorylation, reactive oxygen species, and HIF−1 signaling pathway, were strongly impacted by the BCP + Laser [51,52]. Such a phenomenon may be attributed to the more robust binding of responsive released Cu^{+} to succinylated proteins occurring in the TCA cycle, thus leading to the aggregation of succinylated proteins, the loss of iron-sulfur cluster proteins, and inducing proteotoxic stress, ultimately resulting in a much disrupted TCA cycle and significant cuproptosis-related cell death [51,52]. More importantly, the Gene Set Enrichment Analysis (GSEA) (Fig. 5H–J, Figure S21) further confirmed that the BCP and BCP + Laser exhibited pronounced effects in triggering notable regulation on pathways linked to cuproptosis, including reactive oxygen species, carbon metabolism, mitochondrial autophagy, cellular autophagy, and apoptosis. These cuproptosis-related responses induced by BCP + Laser were more significant than those in the BCP group, possibly due to the responsive release of $Cu^{+/2+}$, leading to increased ROS production and thus triggering more severe cuproptosis-related cell death in TNBC. In summary, the RNA-seq results of the gene transcription network in 4T1 cells, influenced by BCP and BCP + Laser, revealed that the molecular mechanism underlying the enhanced tumor suppression effect of BCP primarily involves triggering oxidative stress and cuproptosis-related pathways to induce enhanced TNBC cell death (Fig. 5).

According to the RNA-seq results, the predominant physiological pathways affected by BCP in the 4T1 cells were oxidative stress, protein degradation, and ROS, among others, strongly suggesting that cellular metabolic disorders are induced by copper homeostasis intervention, leading to programmed cell death, especially cuproptosis [53]. Therefore, the TNBC suppression ability of BCP *in vitro* was further verified by live/dead staining and observed under a fluorescence microscope. 4T1 cells in the pH 7.4 group exhibited strong green fluorescence (Calcein-AM, indicating live cells) with undetectable red fluorescence signals (PI, indicating dead cells) (Fig. 6A). Under acidic conditions (pH = 6.5), significantly increased red fluorescence signals are displayed, which may account for the release of $Cu^{+/2+}$ in response to these conditions. Compared to the pH 7.4 group, the pH 7.4 + Laser group also exhibited an increased red fluorescence signal, suggesting a tumor-killing effect from the photothermal therapy (PPT). The BCP exhibited the most

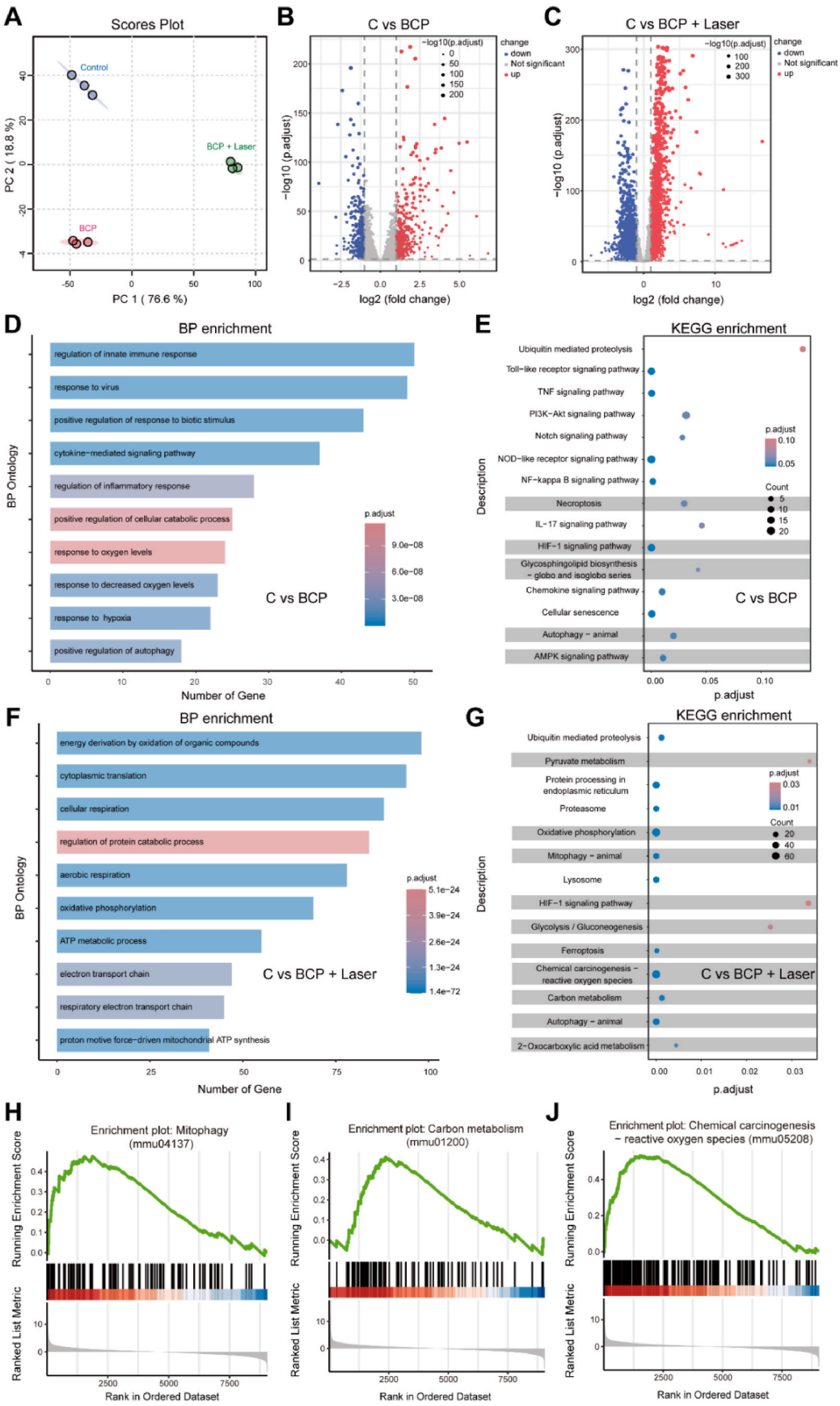

(caption on next page)

Fig. 5. Investigation of the BCP-mediated cuproptosis induction mechanism at the transcriptional level using RNA-seq. (A) PCA analysis of the gene expression profiles of 4T1 cells from different groups (n = 3). (B–C) Volcano plot visually showing the number of upregulated (red dots) and downregulated genes (blue dots) for Control vs. BCP (denoted as C vs. BCP) and Control vs. BCP + Laser (denoted as C vs. BCP + Laser). Cutoff: P-value <0.05 and |log2 FC| > 1. (D) GO enrichment analysis comparing C and BCP. (E) KEGG enrichment analysis of C vs. BCP. (F) GO enrichment analysis of C vs. BCP + Laser. (G) KEGG enrichment analysis of C vs. BCP + Laser. (H–J) GSEA map of the Mitophagy, Carbon metabolism, and reactive oxygen species signaling pathway reveals significant regulation after BCP + Laser treatment of 4T1 cells. (For interpretation of the references to color in this figure legend, the reader is referred to the Web version of this article.)

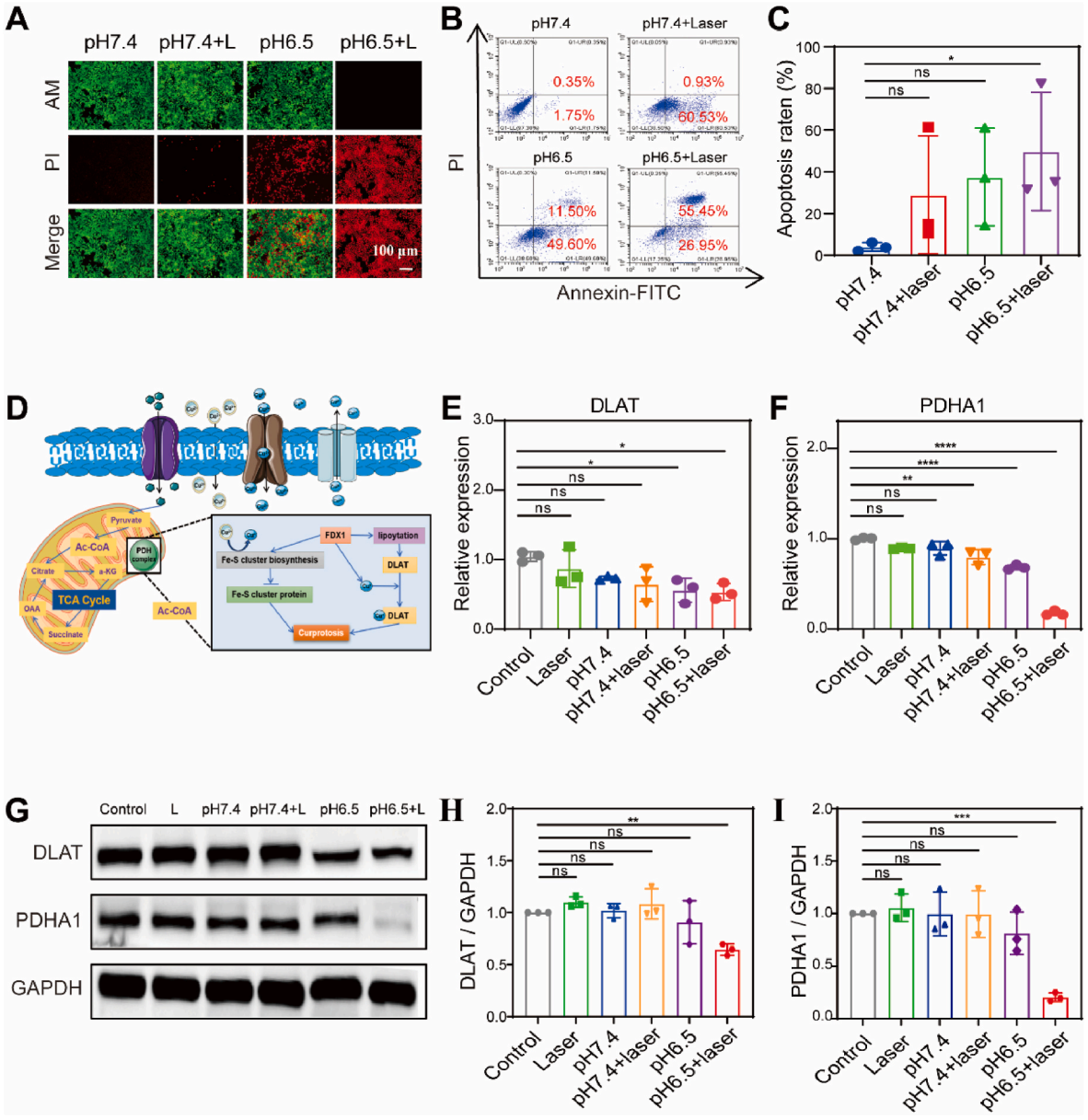

Fig. 6. The cuproptosis induction efficiency of BCP upon acidic pH and laser stimulation *in vitro*. (A) Live-dead staining of 4T1 cells after co-culturing. (B) Apoptosis analysis of 4T1 cells after treatments and (C) related quantification. Data are presented as mean ± S.D., n = 3. (D) Schematic illustration of cuproptosis-related pathways. (E–F) Relative mRNA expression of DLAT and PDHA1, as determined by qPCR. Data are presented as mean ± S.D., n = 3. (G) Relative protein expression of DLAT and PDHA1 by Western blotting and (H–I) related quantification. Data are presented as mean ± S.D., n = 3. Statistics were calculated with the Student's t-test: *: $p < 0.05$, **: $p < 0.01$, ***: $p < 0.001$, ****: $p < 0.0001$. ns, not significant.

notable cell death under pH 6.5 and laser irradiation, demonstrating its synergistic tumor-killing ability in response to the TME and exogenous stimuli.

To further quantify the efficiency of cell death induction by BCP, flow cytometry was used for apoptotic analysis by staining 4T1 cells with Annexin-FITC (green) and PI (red) after treatment (Fig. 6B). Cells under normal conditions (pH = 7.4) showed negligible apoptosis signals. However, the pH 7.4 + Laser group exhibited a significantly elevated early apoptosis rate (60.53 %) and minimal late apoptosis (0.93 %). The potential underlying mechanism causing the appearance of early apoptosis may be that PDA degradation can be instigated not only by the acidic microenvironment but also by a singular photothermal condition. Under the irradiation, the cleavage of molecular bonds, such as hydrogen bonds, within the outermost PDA layer on BCP occurs [54–56]. This process ultimately results in the release of $Cu^{+/2+}$ and subsequently induces cell apoptosis. Such a situation is further

supported by the responsive release profile of copper ions as depicted in Fig. S8, which illustrates that either acidity or photothermal conditions can elicit a responsive release of Cu ions due to the decomposition of PDA. [54–56]. The most pronounced effect was observed in the pH 6.5 + Laser group, which induced both high early apoptosis (55.45 %) and late apoptosis (26.95 %) rates, indicating the efficient and precise killing ability of TNBC triggered by BCP-induced cuproptosis under specific stimulation (Fig. 6C). Such an on-demand therapeutic strategy is primarily attributed to the increased dissolution under acidic conditions and the temperature-dependent disintegration of the dopamine layer modified on BCP, resulting in the rapid release of $Cu^{+/2+}$. These results demonstrate that the PTT evokes the overall anticancer activity of BCP, primarily accounting for cuproptosis and CDT synergistically, which strengthens the notion that BCP is an efficient and precise therapeutic modality for TNBC by inducing cuproptosis.

The molecular mechanism of cuproptosis induced by BCP was further investigated. Cuproptosis is a form of cell death induced by Cu^{+}, distinct from known cell death mechanisms. Excess Cu^{+} can selectively disrupt a subset of enzymes modified by succinylation, inducing related cell death (Fig. 6D). Initially, the expression of cuproptosis-associated genes (DLAT, PDHA1, FDX1, PDHB, etc.) was verified using real-time PCR (qPCR). The results showed that the expression of DLAT, PDHA1 (Fig. 6E and F), and FDX1 (Fig. S12, Supporting Information) is significantly suppressed under acidic and laser stimulation conditions Conversely, PDHB gene expression showed a significant increase upon acidic and laser stimulation (Fig. S22), further verifying the marked and precise induction of cuproptosis by BCP. Then, western blotting is employed to investigate the expression of corresponding marker proteins within the signaling pathways. PDHA1 is a component of the mitochondrial pyruvate dehydrogenase complex, participates in the metabolic process of regulating carbon entry into the tricarboxylic acid (TCA) cycle, and is known to undergo protein succinylation modification. DLAT, an integral part of the TCA cycle, catalyzes specific metabolic reactions and can be directly bound by Cu^{+}, resulting in DLAT heteropolymerization and leading to cuproptosis through cellular proteotoxic stress caused by the insoluble DLAT (Fig. 6D) [15]. Therefore, the expression of these two representative proteins, PDHA1 and DLAT, in cuproptosis was evaluated. The western blotting results show that DLAT and PDHA1 protein expression was also significantly suppressed by BCP under stimulation with acidic pH and laser (Fig. 6G–I) [57,58], consistent with the qPCR results (Fig. 6E and F). Furthermore, the expression of DLAT oligomers was also significantly evaluated in the pH 6.5 + Laser group (Fig. S23), further suggesting the efficient induction of cuproptosis against TNBC [57,58]. Based on the above results, we hypothesize that this may be due to the release of a large amount of monovalent copper ions under acidic and laser conditions by BCP. The released Cu^{+} mediates the aggregation of DLAT and PDHA1 proteins, thereby inhibiting the metabolism of ubiquitinated proteins and leading to cuproptosis in 4T1 cells.

2.5. TNBC inhibition ability of BCP by on-demand cuproptosis-induction *in vivo*

To investigate the *in vivo* biological distribution of BCP, BCP/DIR (100 μL, 1 mg/mL) was administered intravenously to mice, and subsequent NIR-II fluorescence images were captured at various time intervals. As depicted in Fig. S24A, the imaging of BALB/c tumor-bearing mice revealed that the fluorescence signal is predominantly displayed in the tumor regions and increases gradually in a time-dependent manner, possibly due to the structural and functional advantages, such as surface charge [59,60], which is also confirmed by quantitative analysis (Fig. S24B). After 48 h post-injection of BCP/DIR, the main organs and tumors were collected from mice and subjected to *ex vivo* imaging. As shown in Fig. S25A and B, BCP is predominantly accumulated in the liver, spleen, and tumors, thereby underscoring the potent passive tumor-targeting and hepatic clearance capabilities of BCP/DIR NPs, indicating that BCP is degradable and can be metabolized. Collectively, these data substantiate the efficient accumulation of BCP in the tumor regions. Considering BCP is promising in suppressing TNBC by triggering precise cuproptosis under specific stimulation with high therapeutic efficacy and biocompatibility, the *in vivo* anticancer effects are evaluated in TNBC tumor-bearing mice. The establishment of the 4T1 orthotropic tumor model and the therapeutic administration process are illustrated in Fig. 7A. The in-situ temperature in tumor regions of the BCP + Laser group (1.0 W/cm^2) rises rapidly to 50 °C, significantly higher than in the saline, laser, or BCP groups. This result indicates that BCP can effectively accumulate in TNBC tumors via the enhanced permeability and retention (EPR) effect and generate excellent photothermal efficiency under the laser intensity of 1.0W/cm^2, which is sufficient to decompose the PDA to trigger the ion release while maintaining the photothermal temperature at around 50 °C specifically at tumor regions (Fig. 7B and C). The prepared 4T1 tumor-bearing mice were randomly divided into 4 groups. During the treatment process, no significant changes in body weight were observed across all treatment groups (Fig. 7D), indicating the excellent biosafety of BCP. Moreover, after 21 days of treatment, the BCP + Laser group demonstrated the most significant inhibition of TNBC orthotropic tumor (Fig. 7D), with a tumor weight inhibition rate of 85.5 % (Fig. 7E) and tumor volume suppression over 89 % (Fig. 7F), which are much significant than that in mice treated with PBS, Laser or BCP. Furthermore, Ki67 and TUNEL staining also revealed marked tumor necrosis and significantly inhibited tumor growth caused by the combination of BCP and laser (Fig. 7H and I, Fig. S32). Moreover, the immunofluorescence and immunohistochemistry results showed a noticeable DLAT aggregation (Fig. S26A and B) and reduction of PDHA1 (Fig. S27A and B) in the BCP + Laser group, further indicating that the impressive suppression of TNBC tumors is attributed to the precise and on-demand induction of cuproptosis by BCP [61]. The enhanced tumor suppression of TNBC caused by BCP + Laser is also verified by H&E staining of tumors, which reveals a marked necroptosis area (Fig. 7J). More importantly, the application of BCP + Laser caused only negligible toxicity in main organs like the heart (Figs. S16 and S17A), liver (Figs. S28 and S29B), spleen (Figs. S28 and S30A), lung (Figs. S16 and S18B), and kidney (Figs. S28 and S31) collected from 4T1-tumor-bearing mice, suggesting the excellent biosafety of such a precise multifunctional therapeutic modality. Overall, these results demonstrate that the prepared BCP exhibits a potent inhibitory ability against TNBC by triggering specific cuproptosis, as suggested by the correlation analysis of the clinical database, while maintaining excellent biocompatibility.

2.6. Systematic biosafety evaluation of BCP

Although the BCP exhibits impressive TNBC inhibition effects by inducing on-demand cuproptosis, it is crucial to evaluate its systemic toxicity further to examine its potential clinical application. The BCP is administered to healthy mice via tail vein injection for various time intervals (0, 1, 3, 7, 14, and 21 days), as depicted in Fig. 8A. No significant pathological changes are observed in the normal tissues (heart, liver, spleen, lungs, and kidneys) of mice, as determined by H&E staining (Fig. 8B). The blood routine and biochemical parameters examination further revealed that no significant alterations compared to the saline group (Fig. 8C–H) are caused by BCP. These experimental results strengthen the conclusion that the BCP is highly biocompatible. After calculating the hemolysis rate of BCP materials at different concentrations according to Equation (3) in the supporting information, the results were determined, which illustrated that even under the concentration as high as 200 μg/mL, the maximum hemolysis rate of BCP materials was around 2.38 %, significantly lower than the threshold of 5 % for standard hemolysis evaluation [62–64]. Such a measurement on potential hemolysis further indicates that BCP has excellent biocompatibility. (Fig. 8I, Fig. S34). In addition, we incrementally increased the drug dosage to estimate the LD50 value of BCP in mice [60,65,66]. Mice

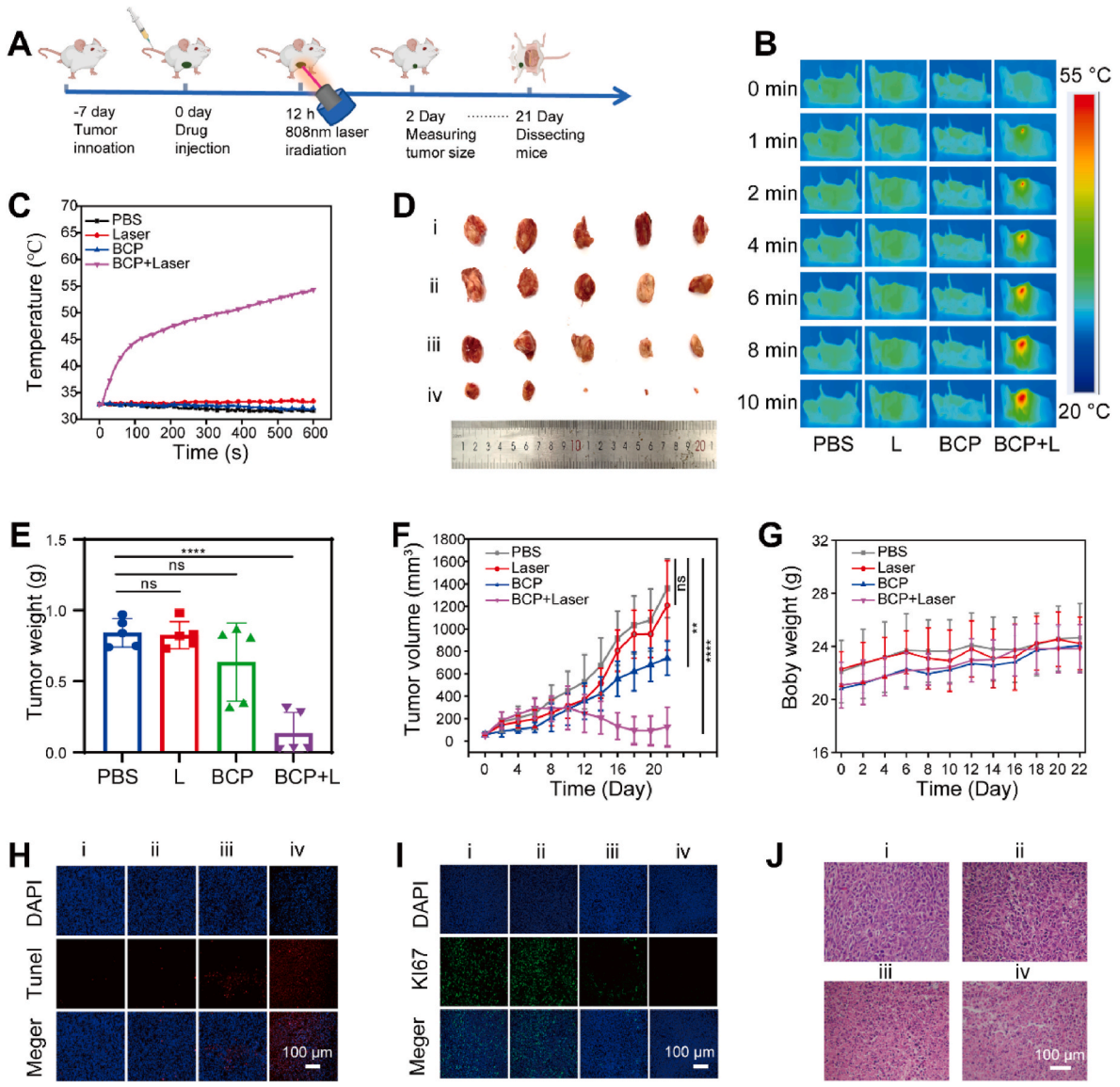

Fig. 7. TNBC inhibition effects conducted by BCP via cuproptosis induction. (A) Schematic illustration of the experimental design. Tumor-bearing mice are subjected to PBS, PBS + Laser, BCP, and BCP + Laser. (B) Photographs of photothermal imaging in mice and (C) their corresponding temperatures. (D) Photographs of collected tumors. (E) Tumor weights, (F) Tumor volumes, and (G) body weights of mice after treatments (n = 5) were calculated from PBS, Laser, BCP, and BCP + Laser groups. (H) Tunel staining and (J) ki67 staining of tumor tissues from the different treatment groups. Scale bar = 100 μm. (J) H&E staining of tumors collected from different groups (on day 21). Scale bar = 100 μm. All Data are shown as mean ± S.D. (n = 5). Statistics were calculated with the Student's t-test: *: $p < 0.05$, **: $p < 0.01$, ***: $p < 0.001$, ****: $p < 0.0001$. ns, not significant.

were intravenously administered with distinct doses of BCP, starting from 700 mg/kg (Table S3). The animals were carefully monitored for signals relating to toxicological responses within the initial 2 h post-administration, followed by additional observations for 6 and 24 h. After 24 h, the mortality rate in each group was meticulously calculated. The dose-dependent mortality of mice in response to BCP is displayed in Table S3, and the corresponding fitting plot of dose versus mortality is shown (Fig. S33) [60,67]. Results indicate that the LD50 value of BCP is approximately 809 mg/kg, which is significantly higher than the therapeutic dosage (5 mg/kg) used in our study. Therefore, the results above further indicate the excellent biocompatibility and safety profile of our TNBC therapeutic modality. In conclusion, these results suggest that BCP causes only a negligible alteration in main organs, blood routine, and biochemical parameters, as well as hemolysis of red blood cells and a much higher LD50 value than therapeutic dosage, emphasizing the low systemic toxicity of BCP, which may be favorable and prospective for clinical applications.

3. Conclusion

The analysis of transcriptional profiles and clinical information conducted by our group revealed that cuproptosis-related transcriptional profiles are highly correlated with the prognosis of TNBC patients. Therefore, cuproptosis-mediated therapy may be an effective candidate for efficiently suppressing TNBC. Thus, a multifunctional cuproptosis-specific inducer (BCP) based on black phosphorus two-dimensional nanosheets (BPNs) is proposed and fabricated. Due to the reducing nature of BPNs, they react with Cu^{2+} to generate Cu^{+}, enabling the high efficiency of Cu^{+} loading. To minimize the unwanted leakage of Cu^{+}, polydopamine (PDA) modification is applied. The obtained BCP can respond to photothermal and acidic pH at the tumor site, thus precisely triggering the release of $Cu^{+/2+}$ with much higher biosafety. Under physiological conditions and without laser irradiation, BCP remains non-toxic ("OFF" state) due to the intact dopamine polymer layer. Specifically, under the stimulation of the acidic tumor microenvironment

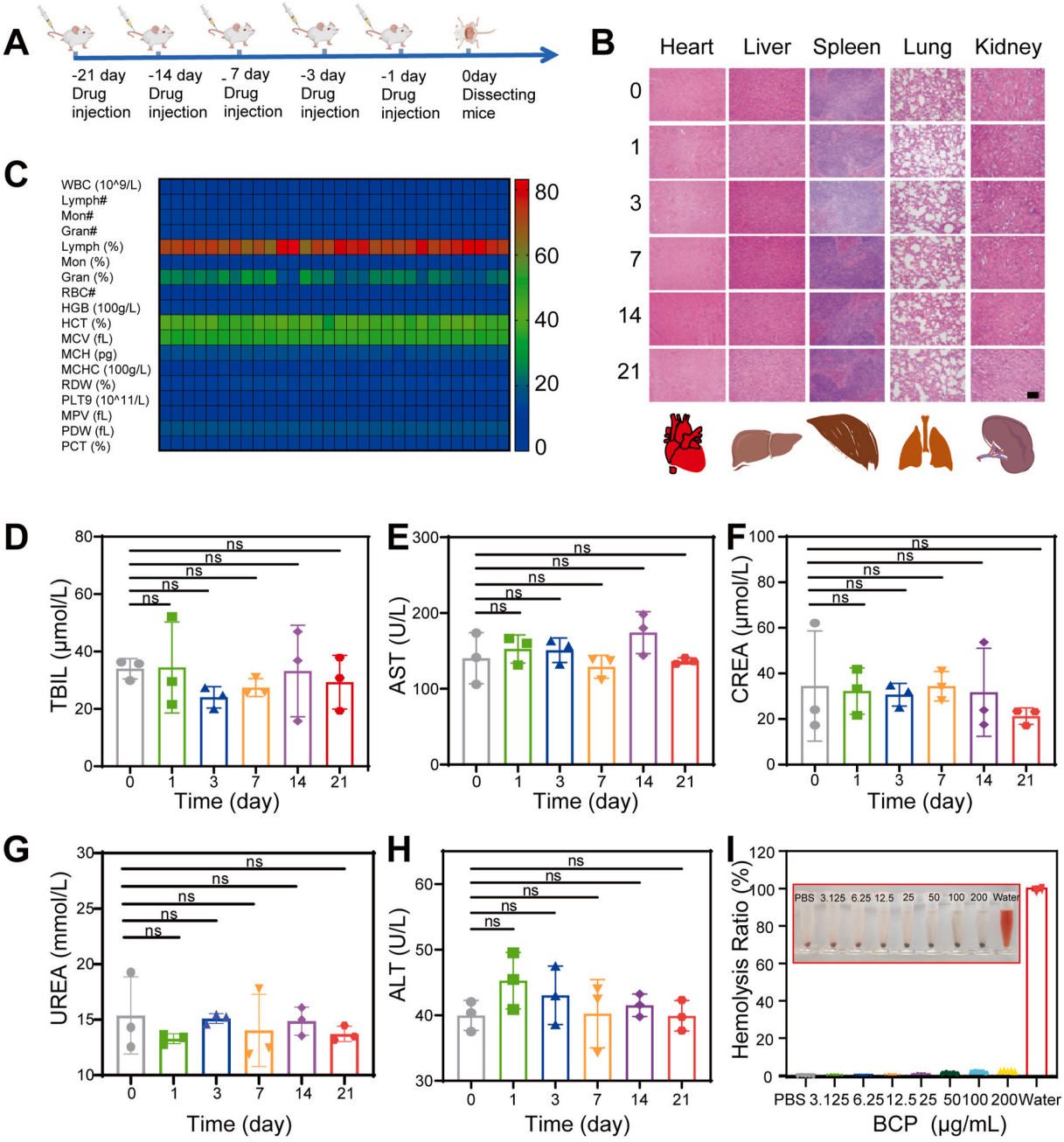

Fig. 8. Systematic evaluation of toxicity caused by BCP. (A) Illustration of the experimental design. (B) H&E staining of the heart, liver, spleen, lung, and kidney collected at different time points (0, 1, 3, 7, 14, and 21 days) (Scale bar = 100 μm). (C) Blood biochemistry of mice after injection of BCP for 1, 3, 7, 14, and 21 days (n = 5). The blood cell counts were compared with those of untreated healthy mice. (D–H) Blood biochemistry data of mice after injection of BCP for 1, 3, 7, 14, and 21 days (n = 3). The blood cell counts and liver and kidney function markers were measured, including TBIL, AST, CREA, UREA, and ALT. (I). Hemolysis rate of red blood cells. Data are shown as mean ± S.D. (n = 5). Statistics were calculated with the Student's t-test: *: $p < 0.05$, **: $p < 0.01$, ***: $p < 0.001$, ****: $p < 0.0001$. ns, not significant. (For interpretation of the references to color in this figure legend, the reader is referred to the Web version of this article.)

and photothermal effects, BCP releases $Cu^{+/2+}$ ("ON" state), enabling the effusive production of ROS from a Fenton-like reaction. The released $Cu^{+/2+}$ further inhibits the TCA cycle, resulting in significantly enhanced TNBC suppression through cuproptosis, which achieves a tumor growth inhibition rate of over 90 % without significant toxicity. In summary, the constructed BCP offers a precise and on-demand TNBC treatment modality as a highly specific inducer of cuproptosis, providing new insights into clinical TNBC intervention strategies based on precise cuproptosis regulation.

CRediT authorship contribution statement

Qiancun Hong: Writing – original draft, Methodology, Investigation, Formal analysis, Data curation, Conceptualization. **Jiajun Huang:** Visualization, Software, Resources, Methodology, Investigation, Formal analysis. **Zhiguo Li:** Validation, Software, Methodology, Investigation, Formal analysis. **Yue Chen:** Methodology, Investigation, Formal analysis, Data curation. **Jiawei Wang:** Software, Methodology, Investigation, Data curation. **Tongrui Shang:** Software, Resources, Methodology, Formal analysis. **Zelin Chen:** Methodology, Investigation. **Cong Luo:** Methodology, Investigation. **Yongqiang Wang:** Methodology,

Investigation. **Xinghong Tang:** Methodology, Investigation. **Taojian Fan:** Software, Resources, Methodology, Formal analysis, Data curation. **Songyin Huang:** Writing – review & editing, Supervision, Resources, Project administration, Funding acquisition. **Hao Fu:** Writing – review & editing, Writing – original draft, Supervision, Methodology, Funding acquisition, Conceptualization. **Yandan Yao:** Visualization, Validation, Supervision, Project administration, Methodology, Funding acquisition, Conceptualization.

Ethics statement

All animal experiments were conducted in accordance with the protocol (AP20230221) approved by the Sun Yat-sen Memorial Hospital Nanhai Laboratory Animal Ethics Committee of Sun Yat-sen University. The housing and experimentation of all animals were strictly carried out in compliance with the institutional guidelines for the care and use of laboratory animals.

Declaration of competing interest

The authors declare that they have no known competing financial interests or personal relationships that could have appeared to influence the work reported in this paper.

Acknowledgments

This research is supported by the National Natural Science Foundation of China (Grant Nos. 82371856, 52302359, 82071859, 82071860), the Foundation of Guangzhou Science and Technology Bureau (Grant No. 2024A03J1055), Guangdong Department of Science and Technology (Grant No. 2024B1212030002), Shanwei Innovation and Entrepreneurship Team Projects (Grant Nos. 2023A012, 2021A005), Guangdong Provincial Clinical Research Center for Breast Diseases (Grant No.2023B110005), the Shanwei Municipal Science and Technology Bureau (Grant No. 2023C017), Science and Technology Projects in Guangzhou (Yat-Sen Excellent Young Scientists Fund, Grant No. 2025A03J4278), Guangdong Province Medical Scientifc Research Foundation (Grant No.B2025836), Science and Technology Planning Project of Guangdong Province (Grant No. 2023B1212060013).

Appendix A. Supplementary data

Supplementary data to this article can be found online at https://doi.org/10.1016/j.mtbio.2025.101985.

Abbreviations

CLSM	Confocal Laser Scanning Microscope
CCK-8	Cell Counting Kit-8
DAPI,4′,6	Diamidino-2-phenylindole
DCFH-DA,2′,7′	Dichlorodihydrofluorescein diacetate
EPR	Enhanced Permeability and Retention
H&E	Hematoxylin and Eosin staining
i.v	intravenous
BCP	BPNs@Cu@PDA
NIR	Near-Infrared
NP	Nanoparticle
PBS	Phosphate-Buffered Saline
PDA	Polydopamine
CDT	Chemodynamic Therapy
PDT	Photodynamic Therapy
PEG	Polyethylene Glycol
PTT	Photothermal Therapy
ROS	Reactive Oxygen Species
TMB	3,3′,5,5′-Tetramethylbenzidine
SD	Standard Deviation
TEM	Transmission Electron Microscope
TME	Tumor Microenvironment
TUNEL	Terminal Deoxynucleotidyl Transferase dUTP Nick-End Labeling
UV	Ultraviolet
XPS	X-ray Photoelectron Spectroscopy

Data availability

Data will be made available on request.

References

[1] E. Nolan, et al., Cell 186 (8) (2023) 1708.
[2] A.G. Waks, E.P. Winer, JAMA 321 (3) (2019) 288.
[3] R. Yerushalmi, et al., Ann. Oncol. 20 (11) (2009) 1763.
[4] J.E. Lang, et al., Ann. Surg Oncol. 20 (2013) 1893.
[5] M T Amjad, A Chidharla, A Kasi, Cancer chemotherapy[J] (2020).
[6] R. Baskar, et al., Int. J. Med. Sci. 9 (3) (2012) 193.
[7] J. Ma, et al., Exploration 3 (5) (2023) 20220161.
[8] X. Bai, et al., Exploration 5 (1) (2025) 20240002.
[9] L. Chen, et al., Signal Transduct. Targeted Ther. 7 (1) (2022) 378.
[10] D. Tang, et al., Cell Res. 32 (5) (2022) 417.
[11] D. Tang, et al., Nat. Rev. Clin. Oncol. 21 (5) (2024) 370.
[12] W. Wang, et al., ACS Nano 17 (20) (2023) 19581.
[13] J. Xie, et al., Mol. Cancer 22 (1) (2023) 46.
[14] T.-J. Zhou, et al., Biomaterials 300 (2023) 122205.
[15] P. Tsvetkov, et al., Science (New York, N.Y.) 375 (6586) (2022) 1254.
[16] I. Martínez-Reyes, N.S. Chandel, Nat. Commun. 11 (1) (2020) 102.
[17] N. Raimundo, et al., Trends Mol. Med. 17 (11) (2011) 641.
[18] G. He, et al., ACS Nano 18 (12) (2024) 9031.
[19] T. Jiang, et al., ACS Nano (2025).
[20] X. Man, et al., Angew. Chem. 136 (51) (2024) e202411846.
[21] Y. Xu, et al., Adv. Mater. 34 (43) (2022) 2204733.
[22] A.C. Doughty, et al., Materials 12 (5) (2019) 779.
[23] F. Raza, et al., Biomater. Sci. 12 (1) (2024) 57.
[24] Q. Tian, et al., Nano Today 39 (2021) 101162.
[25] X. Wang, et al., Nano Today 35 (2020) 100946.
[26] Y. Luo, et al., Exploration 4 (6) (2024) 20230134.
[28] C. Glorieux, et al., Nat. Rev. Drug Discov. 23 (8) (2024) 583.
[29] F.R. Palma, et al., Oncogene 43 (5) (2024) 295.
[30] J. Tang, et al., Exploration 4 (4) (2024) 20230127.
[31] J. Cadet, et al., Mutat. Res. Fund Mol. Mech. Mutagen 424 (1–2) (1999) 9.
[32] B. Lipinski, Oxid. Med. Cell. Longev. 2011 (1) (2011) 809696.
[33] V. Eswaraiah, et al., Small 12 (26) (2016) 3480.
[34] T. Whiteside, Oncogene 27 (45) (2008) 5904.
[35] A. Hayat, et al., Energy Storage Mater. 59 (2023) 102780.
[36] X. Qian, et al., Mater. Horiz. 4 (5) (2017) 800.
[37] L. Qin, et al., J. Contr. Release 318 (2020) 50.
[38] Hayat, A., et al., (2023) 59, 102780.
[39] Z. Liu, et al., Eur. J. Pharm. Biopharm. 182 (2023) 12.
[40] H. Pan, et al., J. Agric. Food Chem. 68 (9) (2020) 2795.
[41] K. Hu, et al., Nat. Commun. 11 (1) (2020) 2778.
[42] W. Zhai, et al., Nano-Micro Lett. 16 (1) (2024) 115.
[43] G.M. Campo, et al., Glycoconj. J. 20 (2003) 133.
[44] Y. Chen, et al., Adv. Sci. 9 (5) (2022) 2103977.
[45] Y. Zhao, et al., ACS Nano 16 (6) (2022) 9304.
[46] B. Jang, et al., Adv. Drug Deliv. Rev. 98 (2016) 113.
[47] H. Li, et al., MRS Advances 4 (7) (2019) 405.
[48] P. Yang, et al., Chem. Soc. Rev. 50 (14) (2021) 8319.
[49] W. Chen, et al., Matter (2025).
[50] R. Yan, et al., Biomaterials 318 (2025) 123176.
[51] F. Liu, et al., Nat. Commun. 15 (1) (2024) 9004.
[52] Y. Liu, et al., Cancer Cell (2025).
[53] B. Liu, et al., Advanced Materials, 2025 2500337.
[54] J. Qiu, et al., Adv. Mater. 33 (45) (2021) 2104729.
[55] N. Xu, et al., ACS Appl. Mater. Interfaces 14 (14) (2022) 15894.
[56] C. Xue, et al., Angew. Chem. Int. Ed. 60 (16) (2021) 8938.
[57] K. Chen, et al., Nano Lett. 23 (7) (2023) 3038.
[58] W. Chen, et al., Adv. Sci. 10 (33) (2023) 2303694.
[59] Y. Ju, S.J. Kent, Nature Nanotechnology, 2025.
[60] S. Vázquez Torres, et al., Nature (2025) 1.
[61] W. Xu, et al., Adv. Funct. Mater. 32 (40) (2022) 2205013.
[62] K. Amin, R.M. Dannenfelser, J. Pharmaceut. Sci. 95 (6) (2006) 1173.
[63] M.A. Dobrovolskaia, et al., Nano Lett. 8 (8) (2008) 2180.
[64] I.P. Sæbø, et al., Int. J. Mol. Sci. 24 (3) (2023) 2914.
[65] K. Morris-Schaffer, M.J. McCoy, ACS chemical health & safety 28 (1) (2020) 25.
[66] M.A. Randhawa, J Ayub med coll abbottabad 21 (3) (2009) 184.
[67] LD50 Calculator, AAT bioquest. www.aatbio.com/tools/ld50-calculator, 2015.